RESEARCH ARTICLE

ADVANCED
ELECTRONIC
MATERIALS
Open Access

www.advelectronicmat.de

Synergistic Enhancement Mechanism of High Electron Density and Localized Surface Plasmons for Strong Light-Matter Interactions

Hongbo Wang, Yang Wang, Zhi-jun Zhao, Xinchuan Du, Anjun Hu, Miao Zhang, Kai Tang, Ting Zhou, Yuchen Tian, Linmao Qian,* and Xianfu Wang*

2D layered semiconductor materials hold the potential to address the crucial technical challenges of poor signal uniformity and low repeatability of traditional metal plasmonic nanostructures in sensing, which hinder quantitative detection and analysis in molecular detection. However, the ultra-low light absorption efficiency and electronic state density intrinsically result in their inferior sensitivity compared with those of conventional metal plasmonic nanostructures. Therefore, the integration of the classical back-gate modulation strategy and surface plasmon resonance into 2D heterostructures is proposed. This integration aims to control the interaction between the surface sensing material of the heterostructure and target molecules from the perspective of surface electronic state density and optical absorption efficiency. The sensitivity ($\approx 10^{-12}$ M) of as-designed MoS_2/graphene/Ag heterojunction is comparable to that of advanced metal plasmonic nanostructures, and the corresponding enhancement factor (EF, 1.71×10^4) is much higher than that of most heterojunction-based and metal-semiconductor coupled devices. This study uncovers the internal mechanism of the surface plasmon effect and high electronic state density in enhancing light-matter interactions, and provides an alternative avenue for high-performance surface-enhanced devices.

1. Introduction

Surface-enhanced devices, as advanced and ultrasensitive sensing technique to enhance the light-matter interactions, have been applied in a wide variety of fields including single-molecule detection,[1–3] bio-imaging,[4–6] disease diagnosis and therapy,[7–9] environment and food safety evaluation,[10–12] and in situ monitoring of various biological and chemical reactions.[13–15] However, the conventional surface plasmon-enhanced devices still face great challenges in quantification analysis fields, because of the localized electromagnetic (EM) field generated by surface plasmon effect of metal nanostructures is the typical short-range effect (2–10 nm) and exhibits significant EM field gradients, which strongly impacting the signal stability and repeatability of analytes, hindering the practical implementation of surface-enhanced devices.

To address these challenges of surface-enhanced devices, 2D layered semiconducting materials are emerging rapidly as a plasmon-free platform for the next-generation surface-enhanced devices via a charge transfer (CT) based chemical (CM) enhancement mechanism (surface effect).[17–19] Compared to the classical surface plasmon-enhanced devices,[20,21] 2D layered semiconducting materials exhibit unique advantages for surface-enhanced devices. On one hand, the large specific surface area is conducive to the combination of surface atoms with adsorbed probe molecules to form CT complexes, thereby brings stronger CT resonance than the conventional metal plasmonic nanostructures.[22] On the other hand, the atomically-flat surface of 2D layered semiconducting materials allows uniform chemisorption of probe molecules, thus facilitating the acquirement of stable and repeatable surface-enhanced signals.[23] Furthermore, the electronic properties including bandgap (for exciton resonance), polarity (for dipole-dipole interaction), and energy level position (for energy level matching) of 2D layered semiconducting materials are easily tunable via doping and nanostructure engineering, which are benefit to optimize their enhancement performances.[22,24,25] Finally, 2D layered semiconducting materials were demonstrated to have obvious selectivity

H. Wang, Z.-jun Zhao
Department of Intelligent Manufacturing and Equipment
Institute of Smart City and Intelligent Transportation
Southwest Jiaotong University
Chengdu, Sichuan 611756, P. R. China
Y. Wang, X. Du, A. Hu, M. Zhang, K. Tang, T. Zhou, Y. Tian, X. Wang
State Key Laboratory of Electronic Thin Films and Integrated Devices
University of Electronic Science and Technology of China
Chengdu, Sichuan 610054, P. R. China
E-mail: xfwang87@uestc.edu.cn
L. Qian
Tribology Research Institute
State Key Laboratory of Traction Power
Southwest Jiaotong University
Chengdu, Sichuan 610031, P. R. China
E-mail: linmao@swjtu.edu.cn

**ADVANCED
SCIENCE NEWS**

www.advancedsciencenews.com

**ADVANCED
ELECTRONIC
MATERIALS**

www.advelectronicmat.de

for probe molecules due to their difference in polarity, bandgap and energy level position.[23,26]

These irreplaceable advantages of 2D layered semiconducting materials ensure they can serve as promising substrates to enhance the light-matter interactions. However, the ultra-low light absorption efficiency (usually <5%) and electronic state density of 2D layered semiconducting materials intrinsically confine their sensitivity and enhancement factor (EF) in surface-enhanced devices, causing their performances far inferior to that of conventional surface plasmon-enhanced devices. Although various enhancement techniques, such as defect-engineering (plasma treatment or UV/ozone oxidation),[27,28] nanostructure functionalization,[29] phase transition,[30] and strain engineering,[31,32] have been developed to enhance their performances, additional efforts are still needed before it can be routinely used as commercial product. The synergistic role of surface plasmon effect and high electronic state density for enhancing light-matter interactions in 2D van der Waals heterostructures are not well established yet. To achieve ultrahigh sensitivity and reliable 2D surface-enhanced devices, it is impressively pivotal to understand the internal interaction mechanism of the surface plasmon effect and high electronic state density within the heterogeneous interface experimentally and theoretically.

In this work, we demonstrate the gate-tunable plasmon-enhanced (GTPE) 2D van der Waals (vdW) heterostructures constructed by the multilayer MoS_2, monolayer graphene, and Ag nanoparticle (NP) array as an efficient platform for surface-enhanced devices. The synergistic role of the surface plasmon effect and high electronic state density for enhancing light-matter interactions in 2D van der Waals heterostructures were clarified experimentally and theoretically. The electronic state density of superficial graphene can be increased because of the interlayer coupling effect between graphene and the underlying MoS_2, as well as the decreased inherent interfacial Schottky barrier of 2D heterostructures under the action of gate modulation. In addition, the plasmon decays through the plasmon-induced interfacial charge-transfer transition (PICTT) pathway can lead to more hot electrons inject to graphene, thereby further increase its electronic state density,[33,34] which greatly increase the electron transition probability between superficial material and probe molecule. Besides, the inherent weak light absorption of 2D layered semiconducting materials can be overcame due to the surface plasmon effect of noble metal Ag NPs, thus significantly enhance the light-matter interactions.

2. Results and Discussion

2.1. Materials and Fabrication of GTPE Chips

To address the challenges faced by 2D semiconductor materials in terms of surface electronic density and optical absorption efficiency, we propose a synergistic enhancement strategy based on gate-controlled interlayer charge transfer (**Figure 1**a) and localized surface plasmons (Figure 1b). Figure 1c,d shows the schematic diagram and physical image of a GTPE platform consisting of 2D MoS_2/graphene heterostructure, Ag NP array and printed circuit board (PCB). The devices were fabricated on a HfO_2/Si substrate with Cr/Au (5/50 nm) electrodes acting as source and drain electrodes, and bottom p-type Si as a back-gate

electrode. The dielectric HfO_2 film (10 nm) was prepared by an atomic layer deposition (ALD) process. All the MoS_2/graphene heterostructures were prepared by mechanical exfoliation and a sacrificial layer (polyvinyl alcohol, PVA) assisted manual-stacking method. In our devices, Ag NPs with ≈40 nm diameters were randomly dispersed on top of MoS_2/graphene heterostructures through an electrostatic approach (inset of Figure 1e).[35] Figure 1d shows the optical image of the as-fabricated device. The thicknesses of graphene and MoS_2 were defined to be 0.5 nm (monolayer) and ≈3.3 (4-5 layers) by atomic force microscopy (Figure 1f,g), respectively. The prominent Raman signature of graphene at 1580 cm^{-1} (G peak) and 2673 cm^{-1} (2D peak) and MoS_2 at 383 cm^{-1} (E^1_{2g} peak) and 406 cm^{-1} (A_{1g} peak) were clearly observed (Figure 1h,i), which confirm the high quality of MoS_2 and graphene.

2.2. Sensing Strategy of GTPE Chips

The surface-enhanced Raman scattering/spectroscopy (SERS) performances of 2D layered semiconducting materials mainly depend on their electron transition probability, light absorption ability, water, and oxygen sensitivity. In our devices, graphene and MoS_2 were adopted to serve as the basic materials as they are less sensitive to water molecules and oxygen, which is suitable for use in most atmospheric and liquid environments. Compared with other 2D layered semiconductors, the relatively mature preparation technology for wafer-scale graphene and MoS_2 samples is also beneficial to achieve large-scale production.

The electron transition probability rate (w_{lk}) between materials can be expressed by Fermi's golden rule:

$$w_{lk} = \frac{2\pi}{\hbar} g\left(E_k\right) \left|H'_{kl}\right|^2 \tag{1}$$

where $g(E_k)$ is the density of states, and H'_{kl} is the matrix element for the highest-occupied molecular orbital orbital (HOMO)–lowest-unoccupied molecular(LUMO) transition which can be perturbed by dipole–dipole interactions between 2D semiconductors and probe molecules. Generally, increased matrix element H'_{kl} is usually demonstrated in strong polar materials including hexagonal boron nitride (h-BN) and ReO_xS_y thin film.[36] For weak polar materials, such as graphene and transition metal dichalcogenides (TMDs), chemical/physical doping and artificial defect are the effective methods to increase their polarity.[27,28,37,38] However, these approaches often cause inevitable damages on the material surface, which is harmful to further regulate their SERS properties through electrical methods. Conversely, the density of states $g(E_k)$ of 2D semiconducting materials can be increased through nondestructive methods, such as heterostructures and plasmon decays.[39,40] Compared with the independent 2D semiconductors, the heterostructure can increase the electronic state density of superficial material through the interlayer coupling effect. Besides, the heterostructure strategy also provide an ideal approach for the mutual complementarity of various 2D semiconductors, thereby give full play to their respective advantages. These unique properties enable the heterostructures to become a potential solution for fabricating high-performance 2D SERS platform through increasing the electronic state density $g(E_k)$.
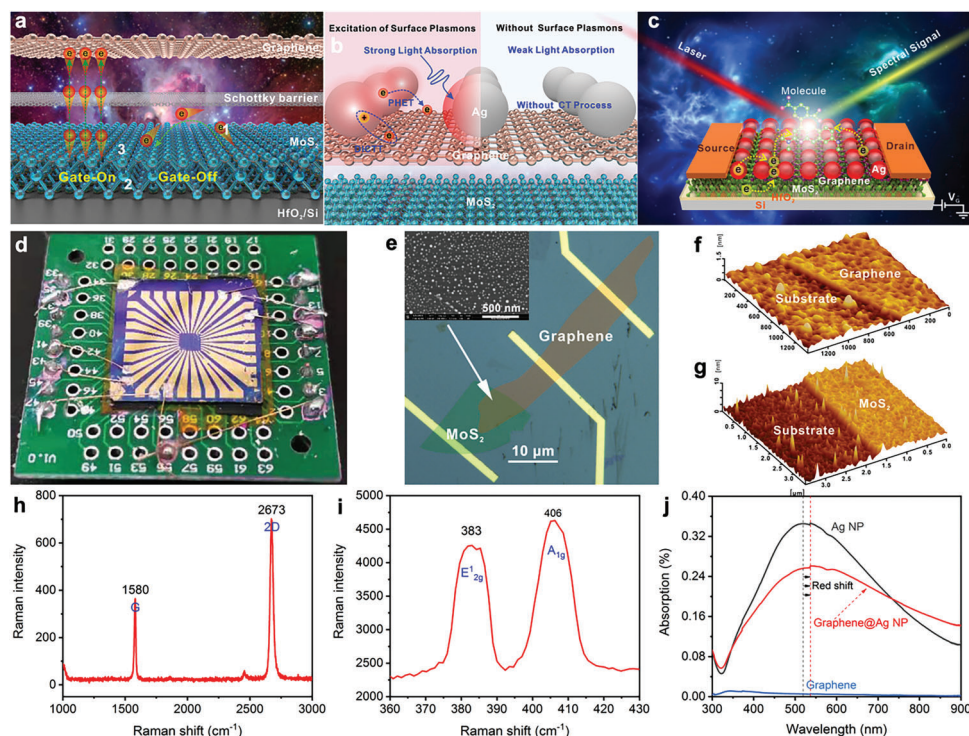
ADVANCED
SCIENCE NEWS
www.advancedsciencenews.com

ADVANCED
ELECTRONIC
MATERIALS
Open Access
www.advelectronicmat.de

Figure 1. Fabrication and sensing strategy of GTPE chip. a) Schematic diagram of interlayer CT transition and back-gate effect in MoS$_2$/graphene heterostructures. b) Interface physical performance differences under the condition of surface plasmons excitation and without surface plasmons. c,d) Schematic diagram and physical image of a 2D GTPE chip. e) Microscopic optical image of an as-fabricated MoS$_2$/graphene heterostructure. The inset is the SEM image randomly dispersed Ag NP array on heterostructure surface. f,g) Atomic force microscopy images of monolayer graphene ($\approx$0.5 nm) and multilayer MoS$_2$ ($\approx$3.3 nm); h,i) Raman spectrum of monolayer graphene and multilayer MoS$_2$. j) Transmission absorption properties of monolayer graphene, Ag NP array, and Ag NP array covered monolayer graphene.

The enhancement magnitude of 2D heterostructure based SERS mainly depends on the superficial material due to the surface effect. For the as-designed heterostructure, graphene was chosen as top material because of its large electronic state density as well as the appropriate Fermi level located near the HOMO (highest-occupied molecular orbital) and LUMO (lowest-unoccupied molecular orbital) of the most probe molecules, which significantly increase the electron transition probability. In addition, graphene can combine with most adsorbed probe molecules to form CT complexes, thus greatly increases the transfer speed and efficiency of carriers. 2D MoS$_2$ was used as the underlying material due to its abundant electronic state providing additional electrons source for superficial graphene and sensitivity to gate regulation.

It's noteworthy that the inherent Schottky barrier (SB, Φ_{SB}) formed at the interfaces between 2D semiconductor materials (Figure 1a) usually reduces the spontaneous interlayer CT, contributing highly to the final electronic state density of superficial graphene. To this end, gate modulation was explored. The ideal schematic band diagrams of as-fabricated 2D heterostructure under gate-on and gate-off mode. A driving force (0.54 V) facilitating electrons transfer from MoS$_2$ to graphene exists at the interface when graphene contact with MoS$_2$, since the work function of pristine graphene is 4.9 eV,[41] while MoS$_2$ is $\approx$4.36 eV.[42] Positive gate bias will induce electrons in MoS$_2$ and decrease its work function, Φ_{MoS2}, such that the SB height between MoS$_2$ and

graphene, $\Phi_{SB} = \Phi_{MoS2}$-Φ_G, is lowered.[41] Hence, more electrons in underlying MoS$_2$ can transfer into graphene and then significantly increase its electronic state density.

Light absorption of the SERS platform plays a crucial role in the final enhancement performance of SERS which is essentially a light-matter interaction. However, the light absorption of 2D semiconducting materials and their heterostructures is much less than that of the metal nanostructures, causing relatively low responsibility. To maximize the light absorption ability of the 2D heterostructure-based SERS platform, we prepared a layer of randomly dispersed Ag NP array on the heterostructure surface through an electrostatic approach, as shown in Figure 1b.[35] In comparison with the pristine MoS$_2$/graphene heterostructure, the light absorption of Ag NP array coupled heterostructure can be greatly enhanced through the local surface plasmon (LSP) effect. As shown in Figure 1j, the monolayer graphene only shows $\approx$1% absorption for UV to near-infrared spectrum, which is largely increased when Ag NP array was introduced. For frequently used lasers with wavelength of 532, 633, and 785 nm, the light absorption efficiency of graphene@Ag NP heterostructures can reach up to $\approx$25.7%, 24%, and 17.4%, respectively. Given that 532 nm excitation wavelength is beneficial to achieve strong light absorption and molecular resonance (R6G),[43] thus 532 nm laser is used to characterize the SERS performances of GTPE devices.

Except for the strong light absorption, the plasmon of Ag NPs can provide additional hot electron source for superficial
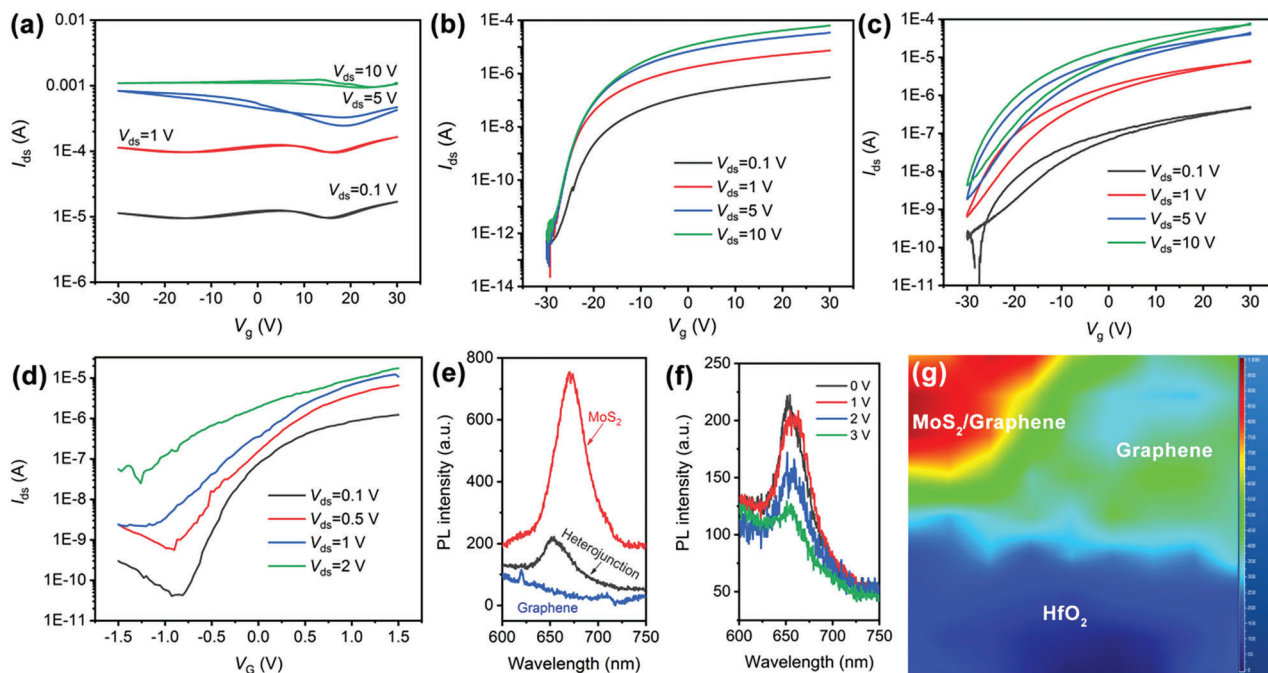
2300454 (3 of 10)

**ADVANCED
SCIENCE NEWS**

www.advancedsciencenews.com

**ADVANCED
ELECTRONIC
MATERIALS**

www.advelectronicmat.de

Figure 2. a–c) Transfer curves of monolayer graphene, multilayer MoS_2, and MoS_2/graphene heterostructure on Si/SiO$_2$ substrates with increased source-drain bias V_{ds} from 0.1–10 V. d) Transfer curves of MoS_2/graphene heterostructure on Si/HfO$_2$ substrate with increased source-drain bias V_{ds} from 0.1–2 V. e) Typical PL spectra of the MoS2, Graphene, and MoS_2/graphene heterostructure. f) Gate-dependent PL spectra of the MoS2/graphene heterostructure with 1 V source-drain bias. g) Raman Mapping of MoS_2/graphene heterostructure on Si/HfO$_2$ substrate with 1 V source-drain bias and 3 V gate bias.

graphene (Figure 1b) through the surface plasmon decays as the plasmon-induced interfacial CT transition (PICTT) and hot electron transfer (PHET) pathways can inject the hot electrons into the adjacent semiconductor materials. In addition, the surface plasmon decays also explains the phenomenon that the light absorption of graphene/Ag NP heterostructures is lower than that of the pure Ag NPs. The light absorption of metal NPs and nanostructures depends on the enhanced electric field amplitude $E(\omega)$ of surface plasmon, which is closely related to the number of hot electrons.[16] Hence, according to the classical electromagnetic theory, once the hot electrons are injected into the nearby graphene through plasmon decay pathways, the intensity of surface plasmon would be decayed by a factor of $|E(\omega)|$.[4]

2.3. Electrical Regulation of Heterojunctions

Gate modulation plays a key role in decreasing the interface Schottky barrier of MoS_2/graphene heterojunction to maximize the electronic state density of graphene. Hence, we first investigated the gate bias sensitivity of monolayer graphene and multilayer MoS_2 through their transfer curves (**Figure 2**a,b). As the V_g step increases from −30 to 30 V, the transfer characteristic of graphene shows little changes, while the drain current (I_{ds}) of multilayer MoS_2 is increased ≈6–8 orders of magnitude.

To confirm the feasibility of gate-tunable MoS_2/graphene heterojunction in increasing the electronic state density of superficial graphene, transfer characteristics were evaluated as typically illustrated in Figure 2c. Compared with pure multilayer

MoS_2, the I_{ds} of MoS_2/graphene heterojunctions show four-fold enhancement when V_g step increases from −30 to 30 V at constant V_{ds}, demonstrating excellent gate bias sensitivity. It's noted that if we swapped the position of graphene and MoS_2, the graphene/MoS_2 heterojunction exhibits poor V_g sensitivity, as demonstrated in Figure S1 (Supporting Information). Since the electron density of underlying graphene (semimetal) is extremely high, the electric field transmitted to MoS_2 is significantly screened.[41]

To further increase the V_g sensitivity of the device, MoS_2/graphene heterojunctions with 10 nm HfO$_2$ dielectric layer coated on silicon substrate was fabricated due to its higher dielectric constant k (25) than that of SiO$_2$ (3.9), which induces higher equivalent oxide thicknesses (EOT, EOT = t_{HfO2} (k_{SiO2}/k_{HfO2})),[44] thereby achieving stronger field regulation with negligible leakage currents. As typically shown in Figure 2d, the I_{ds} of heterojunction increases ≈35-fold when the gate bias increases from 0 to 1.5 V under 1 V V_{ds}. Besides, the V_{ds} applied on the heterojunctions shows obvious effects on the V_g sensitivity. For instance, as the V_{ds} is below 1 V, the I_{ds} of the device is enhanced ≈16, 43, and 35-fold under V_{ds} of 0.1, 0.5 and 1 V, respectively. Such enhancement mainly comes from the reduction of interface Schottky barrier. However, with the V_{ds} further increases to 2 V, the V_g sensitivity of heterojunction is only about nine-fold. Such significant decrease can be attributed to the so-called drain induced barrier lowering effect (DIBL). Hence, 10 nm-thick HfO$_2$ is used as the dielectric layer and 1 V source-drain bias was applied on heterojunctions to achieve optimal V_g sensitivity and maximum electron density.
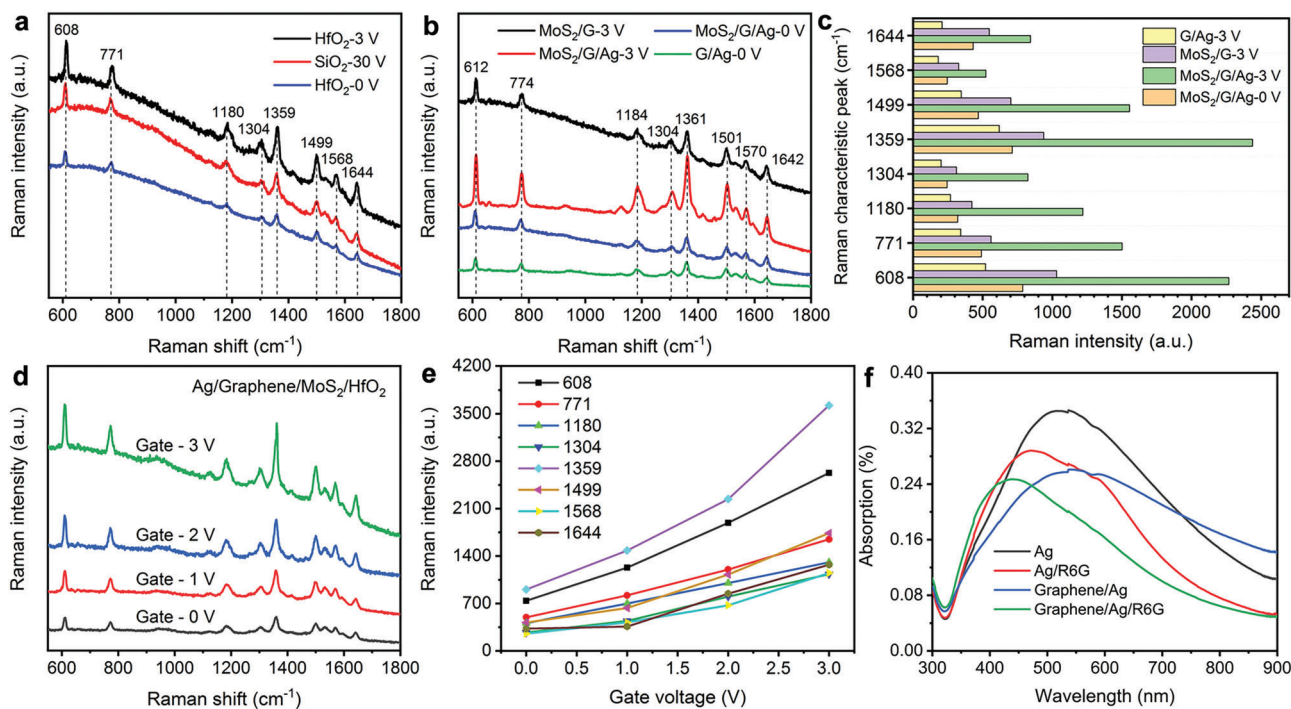
Figure 3. Performance comparison of SERS devices with different configurations. a) Influences of the dielectric layer and gate bias on the SERS performance of MoS$_2$/graphene heterojunctions. b,c) SERS performance comparation of Ag modified graphene and MoS$_2$/graphene heterojunction and pure MoS$_2$/graphene heterojunction. d) SERS spectrum of R6G molecules on MoS$_2$/graphene/Ag heterojunctions under 0–3 V gate bias. e) Correlation of Raman intensity of all the enhanced characteristic peaks and gate bias. f) Transmission absorption spectrum of Ag NP array, Ag NP array covered monolayer graphene (graphene/Ag), R6G molecules modified Ag NP array and graphene/Ag heterojunction.

The interlayer CT of the MoS$_2$/graphene heterojunction under electrical regulation was further verified by characterizing the photoluminescence (PL) spectrum of the samples. As displayed in Figure 2e, a prominent PL peak can be found at ≈670 nm (red line) for multilayer MoS$_2$, corresponding to the direct interband recombination of the electron-hole pairs. In contrast, graphene does not show a representative PL peak within 600–750 nm (blue line). These data are consistent with current research conclusions.[45] Interestingly, the PL intensity of MoS$_2$ is significantly quenched for the MoS$_2$/graphene heterostructures (black line), confirming the transfer of electrons into graphene and reduced electron-hole recombination in the MoS$_2$. As we applied gate bias on the MoS$_2$/graphene heterojunction, the intensity and position of the PL peak produce obvious changes (Figure 2f). On the one hand, as the gate bias gradually increases from 0 to 3 V, the PL peaks of MoS$_2$ in heterostructures change from 670 to 654 nm, exhibiting a large blueshift compared to that of the pristine MoS$_2$ (670 nm). Such position shifts indicate strong interlayer coupling between the graphene and MoS$_2$ layers under gate bias.[46] On the other hand, the PL intensity of MoS$_2$ is decreased ≈10%, 29%, and 45% with the applied gate bias increases to 1, 2, and 3 V, respectively, implying strong modulation of the electron injection in MoS$_2$/graphene heterojunction. Namely, the electronic state density of heterojunction can be increased by controlling the gate bias applied on the heterostructures.

As discussed above, the transfer characteristics and PL results of 2D MoS$_2$/graphene heterojunctions all explain feasibil-

ity and controllability of the gate-tunable strategy in increasing electronic state density, and these electrons can further transfer into the graphene through the strong interlayer coupling, which can largely enhance the SERS performance. As shown in Figure 2g, after immerging the MoS$_2$/graphene heterojunctions into 10^{-5} M R6G solution for 30 min followed with subsequent drying, we characterized the SERS signal by using visualized Raman mapping mode. Compared with the pristine graphene and MoS$_2$, R6G molecules exhibits stronger SERS signal intensity on MoS$_2$/graphene heterojunction. Namely, the interlayer CT in MoS$_2$/graphene heterojunction produces a significant contribution to the final SERS enhancement, demonstrating that the as-proposed interlayer CT regulation strategy for SERS enhancement is effective and reliable, and is expected to increase the sensitivity of 2D layered semiconducting materials.

2.4. SERS Performance of GTPE MoS$_2$/Graphene Heterojunctions

SERS signals of heterojunctions under different conditions using 10^{-5} M R6G probe molecule were systematically analyzed. As shown in **Figure 3**a, compared with the unregulated MoS$_2$/graphene heterojunction (blue line), the SERS signals of MoS$_2$/graphene heterojunctions under gate bias show about two and three-fold enhancement on HfO$_2$ and SiO$_2$ substrates, respectively. These results are consistent with the influence rule of
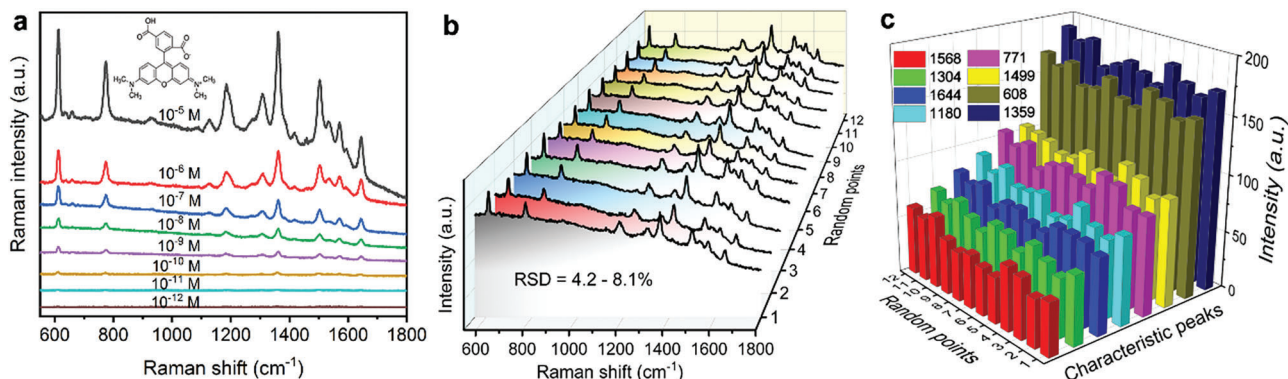
**ADVANCED
SCIENCE NEWS**

www.advancedsciencenews.com

**ADVANCED
ELECTRONIC
MATERIALS**

www.advelectronicmat.de

Figure 4. Sensitivity and repeatability of MoS$_2$/graphene/Ag heterojunctions. a) SERS spectra of R6G molecules with different concentrations. b) SERS spectra of random points on the same substrate (10^{-9} M R6G). c) Histogram of SERS signal intensity of characteristic peaks collected from the Raman spectra of random points.

the high-*k* dielectric layer and back-gate effect on the electronic state density of heterojunctions.

As demonstrated above, the randomly dispersed Ag NP array on the heterostructure surface can increase the light absorption through an electrostatic approach and thus improve the SERS performance. As verified in Figure 3b, the Raman signal strength of the MoS$_2$/graphene/Ag heterojunctions is as high as that of the graphene/Ag devices in the absence of electrical regulation. Once 3 V gate bias was applied on MoS$_2$/graphene/Ag heterojunctions, the Raman signals of probe molecules were significantly enhanced (red line), which are also stronger than that of gate-tunable MoS$_2$/graphene heterojunctions (black line), implying a strong coupling effect between Ag NPs based surface plasmon and graphene with high electronic state density. These performance differences are almost reflected in all characteristic peaks as displayed in Figure 3c.

Gate dependence was then investigated to further confirm the coupling effect. As demonstrated in Figure 3d–e, the SERS signal intensity of all characteristic peaks in the Raman spectra of probe molecules increase obviously with the gate bias ranged from 0 to 3 V. These results verify that the gate-modulated electronic state density plays a key role in the coupling enhancement effect of 2D heterojunctions. Hence, the strong coupling effect between surface plasmon and graphene with high electronic state density provide an ideal approach for enhancing the SERS performance of 2D heterojunctions. Such strong coupling interaction also can be observed from the transmission absorption spectra of Ag NP array, Graphene/Ag heterojunction, R6G molecules modified Ag NP array and Graphene/Ag heterojunction. As shown in Figure 3f, compared with pure Ag NP array, the Graphene/Ag heterojunction exhibits red-shift, lower and broader absorption within the whole visible-light range, indicating strong interfacial coupling interaction that induced by the PICTT and PHET effects was generated between graphene and Ag NPs. Significantly, such interfacial coupling interaction still exists and becomes more stronger when the heterojunction was modified by R6G molecules, because of the R6G/Ag/graphene heterojunction shows a bigger blue-shift than that of R6G/Ag sample. These results reveal the strong coupling interaction between surface plasmon and hot electrons in enhancing the light-matter interaction.

Limit of detection (LOD) and relative standard deviation (RSD) are the key parameters for SERS devices. Then the LOD of MoS$_2$/graphene/Ag heterojunctions was evaluated by performing experiments in R6G molecular solution with different concentrations. As the concentration of R6G decreases from 10^{-5} to 10^{-12} M, the signal intensity of "fingerprint" spectra acquired from MoS$_2$/graphene/Ag heterojunctions (V_{ds} = 1 V, V_g = 3 V) shows an obvious attenuation due to the decrease of captured probe molecules (**Figure 4**a). But the "fingerprint" feature of R6G molecules can still be clearly distinguished when the concentration of R6G solution decreased to 10^{-11} and 10^{-12} M, as shown in Figure S2 (Supporting Information). Hence, the LOD of gate-tunable plasmon-enhanced MoS$_2$/graphene/Ag heterojunctions in detecting R6G probe molecules can reach to ≈10^{-12} M. This value is much higher than most 2D semiconducting materials, even is comparable to many advanced EM enhanced SERS devices.[47–49] To better evaluate their SERS performance, we further characterized the spot-to-spot reproducibility of MoS$_2$/graphene/Ag heterojunctions after treating them in 10^{-9} M R6G solution (Figure 4b). According to the statistical analysis from 12 random points, the RSD is as low as 4.2%, and even for all characteristic peaks, the maximal RSD only shows 8.1% variation, as presented in Figure 4c. Such low RSD is better than that of current metal nanostructure-based SERS devices (usually ≈15%). In addition, by comparing the SERS intensity of R6G molecules on the gate-tunable MoS$_2$/graphene/Ag heterojunctions (I_{SERS}) to the Raman intensity of the pure R6G solution (I_{RS}), the EF value of the device was calculated to be ≈1.71 × 10^4 (Section S1, Supporting Information), which is much higher than that of most heterojunction-based and metal-semiconductor coupled SERS devices (usually in the range of tens to hundreds).[21]

2.5. Enhancement Mechanisms of Gate-Tunable Plasmon-Enhanced MoS$_2$/Graphene Heterojunctions

Two main enhancement mechanisms can be summarized based on proposed enhancement strategies and previous experimental results for gate-tunable plasmon-enhanced MoS$_2$/graphene heterojunctions. On the one hand, light absorption efficiency of
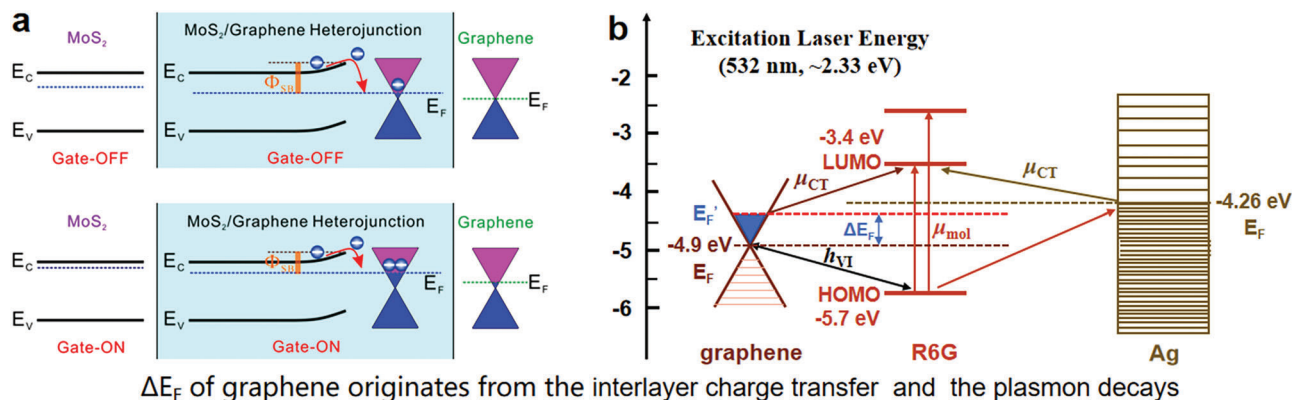
Figure 5. a) Schematic band diagrams of interlayer charge transfer transition and back-gate effect in 2D heterostructures. b) Energy-level diagram and charge transfer transitions. μ_{CT}, μm_{ol}, and h_{VI} denote charge transfer transition resonance, molecular transition resonance and the Herzberg–Teller constant, respectively.

devices is greatly increased through surface plasmon effect induced by additional Ag NPs, which enhances the light-matter interactions and provides additional hot-electron injection into graphene. On the other hand, the gate-tunable interlayer interactions increase the electronic state density of top sensing 2D semiconducting material via enhancing the CT at the interface, thereby improving the Raman scattering of the probe molecule on the surface.

Figure 5a shows the schematic band diagrams of as-fabricated 2D heterostructure under gate-on and gate-off mode. Due to the back-gate effect reduce the Schottky barrier in the heterojunction, more electrons can be facilitated to transfer to the surface of graphene through interlayer charge transition. Consequently, the electron concentration of graphene increases, leading to an elevation in the actual work function from E_F (-4.9 eV) to E_F'. The magnitude of ΔE_F is directly related to the practical extent of charge transfer. Beyond interlayer charge migration, the hot electrons stemming from the decay of surface plasmon resonance on Ag NPs can also contribute to ΔE_F by engaging in the PICT process to access the neighboring graphene surface.

As shown in Figure 5b, the increment of actual work function in graphene can diminish the charge transfer barrier (<1.5 eV) between the LUMO of R6G molecules and graphene, subsequently significantly enhancing the probability (w_{lk}) of charge transfer (μ_{CT}). Moreover, the PICT process is also plausible to occur between Ag nanoparticles and R6G molecules due to the energy barriers existing between the LUMO, HOMO of R6G and the Fermi level of Ag are -1.14 and -1.44 eV, respectively. Considering the excitation laser energy (≈ 2.33 eV), it adequately satisfies the energy requisites for the transition process. In contrast, the molecular resonance for R6G's intrinsic transitions might be exceedingly weak, as the energy barrier between its LUMO and HOMO molecular orbitals is ≥ 2.3 eV, aligning closely with the excitation laser energy. In a word, these PICT resonances can affect the distribution of the electric cloud of R6G molecules, thereby increasing its polarization and enhance the sensing signal.

To further clarify the role of electronic state density for enhancing light-matter interactions, the influence of electronic

state density on the interaction strength and CT behavior between graphene and probe molecules was then analyzed using the density functional theory (DFT). Theoretically, strong physisorption interactions rather than strong chemical process exisits between the perfect graphene and R6G molecules with calculated adsorption energy ≈ 1.77 eV. However, the absorption spectrum results indicate that there are strong chemical interactions between the graphene and R6G molecules as the resonance peak generates a remarkable blue shift from 547 to 429 nm after the Ag@graphene substrate was functionalized by R6G molecules (Figure 3f). The graphene used in our experiments may be artificially formed obvious vacancy defects during the preparation process of heterojunctions. These vacancy defects provide ideal anchors for the $-NH_3$ of R6G molecules, which induces the polarizability through enhancing the CT process and thus improve the SERS performances. To simplify the analysis, physisorption of R6G molecules on graphene was considered to unveil the universal influence of electronic state density on the CT behavior and polarization (**Figure 6**a). The detailed methods are listed in the Section S2 (Supporting Information).

As shown in Figure 6b,c, the interaction region indicator (IRI) results indicated that the interaction strength generated by van der Waals force and π-hydrogen bond between monolayer graphene and R6G molecule almost without change even the number of electron injection of graphene increase from 0 to 2. Namely, for physisorption, the interface interaction strength almost does not increase with the electronic state density of monolayer graphene. The R6G/graphene system is still noncovalent interactions. However, Figure 6d,e indicated that either vertical contact mode (R6G-V) or plane contact mode (R6G-P), the electrons in monolayer graphene all tend to gather near R6G molecules. According to Fermi's golden rule, such local capture effect of electrons can directly increase the electron transition probability rate. Furthermore, the local capture effect also induces the polarization of R6G molecule, and the polarization strength of R6G molecule increase with electronic state density of graphene. Fermi's golden rule indicate that such polarization enhancement is conducive to increase the electron transition probability rate in R6G/graphene system.
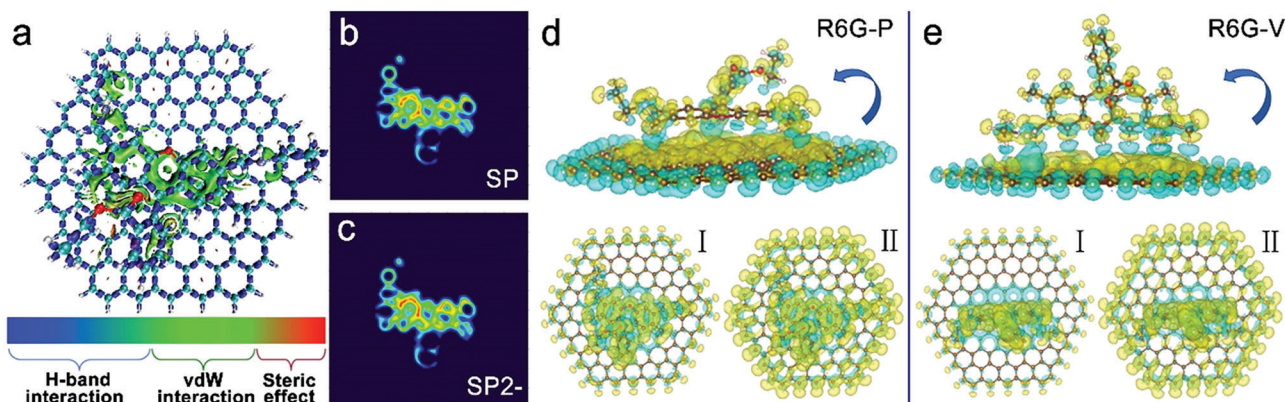
Figure 6. a) The 3D visual molecular dynamics (VMD) result shows the electrostatic potential distribution of the R6G molecule on the graphene surface. b,c) The influence of electronic state density on the interfacial interaction. (interaction region indicator, IRI).[50] d,e) The influence of electronic state density on the difference charge density of R6G-P/graphene and R6G-V/graphene system. The yellow zones represent the increase of charge density while the blue zones represent the decrease of charge density. Among, the (I) and (II) show the difference charge density results after applying 1 and 2 electrons to the carbon atoms of graphene, respectively.

Hence, the performance enhancement of our devices induced by high electronic state density may be through the local capture effect of electrons and polarization enhancement pathway of molecules rather than the changes in interface interaction strength.

3. Conclusion

In summary, the effectiveness of the GTPE MoS$_2$/graphene heterojunction in enhancing light-matter interactions has been convincingly demonstrated experimentally and theoretically. The 2D layered semiconducting materials with low electronic state density and inferior light absorption efficiency confine their sensitivity in surface-enhanced devices, while the surface plasmon effect of Ag nanoparticles as well as the abundant electrons source of 2D heterostructures provide excellent light absorption efficiency and high electronic state density, which act in concert to achieve strong light-matter interactions. In addition, the gate modulation enhances the spontaneous interlayer CT by decreasing the inherent Schottky barrier of 2D heterostructures, then significantly increasing their electronic state density. The GTPE devices with high sensitivity ($\approx 10^{-12}$ M), large enhancement factor (EF, 1.71×10^4), and low RSD (4.2%) have been successfully demonstrated to exhibit strong light-matter interactions and excellent stability. This work elucidates the role of the surface plasmon effect and high electronic state density in light-matter interactions, providing an alternative avenue for the development of other 2D layered semiconducting materials-based surface-enhanced devices.

4. Experimental Section

Materials Preparation: 2D Graphene and MoS$_2$ nanoflakes were mechanically exfoliated from bulk graphene and MoS$_2$ crystal (2D Materials), respectively. Subsequently, they were transferred onto silicon substrates covered with 285 nm-thick SiO$_2$ (MEMC Electronic Materials, Inc., USA) or 10 nm-thick HfO$_2$ (atomic layer deposition, ALD) dielectric layers. ALD of HfO$_2$ was performed using KE-MICRO PEALD-100A system. The ALD chamber was heated to 200 °C, the hafnium precursor

tetrakis(dimethylamino)hafnium (Hf(N(CH$_3$)$_2$)$_4$) (TDMAH) was heated to 80 °C and the H$_2$O source was kept at room temperature. The purge gas was Ar with a flow rate of 100 sccm and the pressure was 0.2 mTorr. The pulse time for TDMAH and H$_2$O were 0.08 and 0.02 s, respectively. The post TDMAH and H2O pulse purge with Ar for 60 s. The growth rate was 1 Å/cycle. The polyvinyl alcohol (PVA) film was made by dissolving solid concentrated PVA (Sinopharm Chemical Reagent Co., Ltd.) in deionized water to form 3% aqueous PVA. After further stirring at 60 °C for 6 h, the aqueous PVA was transferred to a glass petri dish for 24 h.

Fabrication of Heterostructures: The heterostructures were assembled by a sacrificial layer-assisted manual-stacking method, also known as the standard polymer stamp dry-transfer technique. First, a polydimethylsiloxane (PDMS) stamp coated with a thin polyvinyl alcohol (PVA) film was used to sequentially pick up graphene (or MoS$_2$) flakes, flipped over, and transferred onto a clean SiO$_2$/Si (or HfO$_2$/Si) substrate. Second, the sample was annealed in a glovebox at ≈60–80 °C for 3–5 min to remove the PDMS film. Third, after the PVA film was removed by deionized water (30 °C, 30 min), the graphene was successfully transferred onto the SiO$_2$/Si substrate. Finally, based on the same approach, the monolayer graphene (or MoS$_2$) was partially covered by the top multilayer MoS$_2$ (or graphene) flake to form graphene/MoS$_2$ (or MoS$_2$/graphene) heterojunctions.

Device Fabrication and Electric Measurement: The devices were fabricated by standard electron-beam lithography method (JC Nabity, NPGS). Then the Cr/Au (5/50 nm) electrodes were deposited by metal evaporation and standard lift-off processes. Electric characterization was based on PRCBE DOT probe station and Keithley 4200-SCS semiconductor parameter analyzer.

Surface Functionalization of Heterostructures: The aqueous R6G was made by dissolving solid concentrated R6G (Sinopharm Chemical Reagent Co., Ltd.) in deionized water. Different concentrations of R6G solution were made by diluting the highest concentration R6G solution (10^{-5} M). Before Raman experiment, the MoS$_2$/graphene heterostructures were dipped into the analyte solutions to ensure the adsorption–desorption equilibrium between the analytes and MoS$_2$/graphene heterostructure before experiments. Then, the MoS$_2$/graphene heterostructures were immersed in the fresh deionized water for 2 min to remove the redundant molecules and dried with nitrogen gas flow.

Supporting Information

Supporting Information is available from the Wiley Online Library or from the author.

Conflict of Interest

The authors declare no conflict of interest.

Data Availability Statement

The data that support the findings of this study are available from the corresponding author upon reasonable request.

[1] R. B. Jaculbia, H. Imada, K. Miwa, T. Iwasa, M. Takenaka, B.o Yang, E. Kazuma, N. Hayazawa, T. Taketsugu, Y. Kim, *Nat. Nanotechnol.* **2020**, *15*, 105.

[2] N. Maccaferri, G. Barbillon, A. N. Koya, G. Lu, G. P. Acuna, D. Garoli, *Nanoscale Adv.* **2021**, *3*, 633.

[3] A. B. Zrimsek, N. Chiang, M. Mattei, S. Zaleski, M. O. Mcanally, C. T. Chapman, A.-I. Henry, G. C. Schatz, R. P. Van Duyne, *Chem. Rev.* **2017**, *117*, 7583.

[4] R. Zhu, L. Su, J. Dai, Z.-W. Li, S. Bai, Q. Li, X. Chen, J. Song, H. Yang, *ACS Nano* **2020**, *14*, 3991.

[5] D. N. Basov, M. M. Fogler, *Science* **2017**, *357*, 132.

[6] N. C. Lindquist, C. D. L. De Albuquerque, R. G. Sobral-Filho, I. Paci, A. G. Brolo, *Nat. Nanotechnol.* **2019**, *14*, 981.

[7] Q. Fu, X. Zhang, J. Song, H. Yang, *View* **2021**, *2*, 20200149.

[8] J. J. S. Rickard, V. Di-Pietro, D. J. Smith, D. J. Davies, A. Belli, P. G. Oppenheimer, *Nat. Biomed. Eng.* **2020**, *4*, 610.

[9] C. Li, S. Li, A. Qu, C. Xu, L. Xu, H. Kuang, *Small Struct.* **2021**, *2*, 2000150.

[10] T. Yaseen, H. Pu, D.-W. Sun, *Trends Food Sci. Technol.* **2018**, *72*, 162.

[11] J. Yu, J. Wu, H. Yang, P. Li, J. Liu, M. Wang, J. Pang, C. Li, C. Yang, K. Xu, *ACS Appl. Mater. Interfaces* **2022**, *14*, 43877.

[12] T. T. X. Ong, E. W. Blanch, O. A. H. Jones, *Sci. Total Environ.* **2020**, *720*, 137601.

[13] B. Y. Wen, Q. Q. Chen, P. M. Radjenovic, J. C. Dong, Z. Q. Tian, J. F. Li, *Annu. Rev. Phys. Chem.* **2021**, *72*, 331.

[14] K. Xu, H. Yan, C. F. Tan, Y. Lu, Y. Li, G. W. Ho, R. Ji, M. Hong, *Adv. Opt. Mater.* **2018**, *6*, 1701167.

[15] W. Zhang, F. Lin, Y. Liu, H. Zhang, T. A. Gilbertson, A. Zhou, *Proc. Natl. Acad. Sci. USA* **2020**, *117*, 3518.

[16] J. Langer, D. Jimenez De Aberasturi, J. Aizpurua, R. A. Alvarez-Puebla, B. Auguié, J. J. Baumberg, G. C. Bazan, S. E. J. Bell, A. Boisen, A. G. Brolo, J. Choo, D. Cialla-May, V. Deckert, L. Fabris, K. Faulds, F. J. García De Abajo, R. Goodacre, D. Graham, A. J. Haes, C. L. Haynes, C. Huck, T. Itoh, M. Käll, J. Kneipp, N. A. Kotov, H. Kuang, E. C. Le Ru, H. K. Lee, J.-F. Li, X. Y. Ling, et al., *ACS Nano* **2019**, *14*, 28.

[17] Z. Yin, K. Xu, S. Jiang, D. Luo, R. Chen, C. Xu, P. Shum, Y. J. Liu, *Mater. Today Phys.* **2021**, *18*, 100378.

[18] Z. Li, W. Yang, M. Huang, X. Yang, C. Zhu, C. He, L. Li, Y. Wang, Y. Xie, Z. Luo, D. Liang, J. Huang, X. Zhu, X. Zhuang, D. Li, A. Pan, *Opto-Electron. Sci.* **2021**, *4*, 210017.

[19] A. Elbanna, K. Chaykun, Y Lekina, Y Liu, B. Febriansyah, S. Li, J. Pan, Z. Shen, J. Teng, *Opto-Electron. Sci.* **2022**, *1*, 220006.

[20] H. Wang, G. Rao, Y. Wang, X. Du, M. Zhang, X. Wang, A. Hu, Y. Hu, J. Huang, J. Chu, X. Wang, L. Qian, J. Xiong, *J. Phys. Chem. C* **2021**, *125*, 4710.

[21] H. Wang, Y. Liu, G. Rao, Y. Wang, X. Du, A. Hu, Y. Hu, C. Gong, X. Wang, J. Xiong, *Analyst* **2021**, *146*, 5008.

[22] X. Wang, W. Shi, S. Wang, H. Zhao, J. Lin, Z. Yang, M.o Chen, L. Guo, *J. Am. Chem. Soc.* **2019**, *141*, 5856.

[23] X. Song, Y. Wang, F. Zhao, Q. Li, H. Q. Ta, M. H. Rummeli, C. G. Tully, Z. Li, W. J. Yin, L. Yang, K. B. Lee, J. Yang, I. Bozkurt, S. Liu, W. Zhang, M. Chhowalla, *ACS Nano* **2019**, *13*, 8312.

[24] J. Tan, B. Du, C. Ji, M. Shao, X. Zhao, J. Yu, S. Xu, B. Man, C. Zhang, Z. Li, *ACS Photonics* **2023**, *10*, 2216.

[25] L. Tao, Z. Chen, Z. Li, J. Wang, X. Xu, J.-B. Xu, *InfoMat* **2020**, *3*, 36.

[26] S. Huang, X. Ling, L. Liang, Y. Song, W. Fang, J. Zhang, J. Kong, V. Meunier, M. S. Dresselhaus, *Nano Lett.* **2015**, *15*, 2892.

[27] S. Huh, J. Park, Y. S. Kim, K. S. Kim, B. H. Hong, J.-M. Nam, *ACS Nano* **2011**, *5*, 9799.

[28] B. Ananthoju, R. K. Biroju, W. Theis, R. A. W. Dryfe, *Small* **2019**, *15*, 1901555.

[29] V. Thareja, M. Esfandyarpour, P. G. Kik, M. L. Brongersma, *ACS Photonics* **2019**, *6*, 1996.

[30] X. Wang, L. Guo, *Angew. Chem., Int. Ed.* **2020**, *59*, 4231.

[31] S. Yang, Y. Chen, C. Jiang, *InfoMat* **2021**, *3*, 397.

[32] Y. Huang, Y. K. Wang, X. Y. Huang, G. H. Zhang, X. Han, Y. Yang, Y. Gao, L. Meng, Y. Wang, G. Z. Geng, L. W. Liu, L. Zhao, Z. H. Cheng, X. F. Liu, Z. F. Ren, H. X. Yang, Y. Hao, H. J. Gao, X. J. Zhou, W. Ji, Y. L. Wang, *InfoMat* **2021**, *4*, 12274.

[33] Y. Liu, H. Ma, X. X. Han, B. Zhao, *Mater. Horiz.* **2020**, *8*, 370.

[34] Y. Liu, Q. Chen, D. A. Cullen, Z. Xie, T. Lian, *Nano Lett.* **2020**, *20*, 4322.

[35] I. Epstein, D. Alcaraz, Z. Huang, V.-V. Pusapati, J.-P. Hugonin, A. Kumar, X. M. Deputy, T. Khodkov, T. G. Rappoport, J.-Y. Hong, N. M. R. Peres, J. Kong, D. R. Smith, F. H. L. Koppens, *Science* **2020**, *368*, 1219.

[36] J. Seo, J. Lee, Y. Kim, D. Koo, G. Lee, H. Park, *Nano Lett.* **2020**, *20*, 1620.

[37] S. Feng, M. C. Dos Santos, B. R. Carvalho, R. Lv, Q. Li, K. Fujisawa, A. L. Elías, Y.u Lei, N. Perea-López, M. Endo, M. Pan, M. A. Pimenta, M. Terrones, *Sci. Adv.* **2016**, *2*, 1600322.

[38] L. Sun, H. Hu, D. Zhan, J. Yan, L. Liu, J. S. Teguh, E. K. L. Yeow, P. S. Lee, Z. Shen, *Small* **2014**, *10*, 1090.

[39] Y. Tan, L. Ma, Z. Gao, M. Chen, F. Chen, *Nano Lett.* **2017**, *17*, 2621.

[40] M. Shibuta, K. Yamamoto, T. Ohta, T. Inoue, K. Mizoguchi, M. Nakaya, T. Eguchi, A. Nakajima, *ACS Nano* **2021**, *15*, 1199.

[41] C.-J. Shih, Q. H. Wang, Y. Son, Z. Jin, D. Blankschtein, M. S. Strano, *ACS Nano* **2014**, *8*, 5790.

[42] S. Y. Lee, U. J. Kim, J. Chung, H. Nam, H. Y. Jeong, G. H. Han, H. Kim, H. M. Oh, H. Lee, H. Kim, Y.-G. Roh, J. Kim, S. W. Hwang, Y. Park, Y. H. Lee, *ACS Nano* **2016**, *10*, 6100.

[43] J. A. Dieringer, K. L. Wustholz, D. J. Masiello, J. P. Camden, S. L. Kleinman, G. C. Schatz, R. P. Van Duyne, *J. Am. Chem. Soc.* **2009**, *131*, 849.

[44] Y. Y. Illarionov, T. Knobloch, M. Jech, M. Lanza, D. Akinwande, M. I. Vexler, T. Mueller, M. C. Lemme, G. Fiori, F. Schwierz, T. Grasser, *Nat. Commun.* **2020**, *11*, 3385.

[45] X. Guo, R. Liu, D. Hu, H. Hu, Z. Wei, R. Wang, Y. Dai, Y. Cheng, K. Chen, K. Liu, G. Zhang, X. Zhu, Z. Sun, X. Yang, Q. Dai, *Adv. Mater.* **2020**, *32*, 1907105.

ADVANCED
SCIENCE NEWS

www.advancedsciencenews.com

ADVANCED
ELECTRONIC
MATERIALS

www.advelectronicmat.de

[46] W. Zheng, B. Zheng, Y. Jiang, C. Yan, S. Chen, Y. Liu, X. Sun, C. Zhu, Z. Qi, T. Yang, W. Huang, P. Fan, F. Jiang, X. Wang, X. Zhuang, D. Li, Z. Li, W. Xie, W. Ji, X. Wang, A. Pan, *Nano Lett.* **2019**, *19*, 7217.

[47] X. Jin, Q. Zhu, L. Feng, X. Li, H. Zhu, H. Miao, Z. Zeng, Y. Wang, Y. Li, L. Wang, X. Liu, G. Shi, *ACS Appl. Mater. Interfaces* **2021**, *13*, 11535.

[48] J. Xu, H. He, X. Jian, K. Qu, J. Xu, C. Li, Z. Gao, Y. Y. Song, *Anal. Chem.* **2021**, *93*, 9286.

[49] H. Dang, S.-G. Park, Y. Wu, N. Choi, J.-Y. Yang, S. Lee, S.-W. Joo, L. Chen, J. Choo, *Adv. Funct. Mater.* **2021**, *31*, 2105703.

[50] T. Lu, Q. Chen, *Chem. Methods* **2021**, *1*, 231.